

Dynamically preferred state with strong electronic fluctuations from electrochemical synthesis of sodium manganate

X. Chen, E. Hu

To be published in "Matter"

January 2022

Chemistry Department
Brookhaven National Laboratory

U.S. Department of Energy

USDOE Office of Energy Efficiency and Renewable Energy (EERE), Vehicle Technologies Office
(EE-3V)

Notice: This manuscript has been authored by employees of Brookhaven Science Associates, LLC under Contract No. DE-SC0012704 with the U.S. Department of Energy. The publisher by accepting the manuscript for publication acknowledges that the United States Government retains a non-exclusive, paid-up, irrevocable, world-wide license to publish or reproduce the published form of this manuscript, or allow others to do so, for United States Government purposes.

DISCLAIMER

This report was prepared as an account of work sponsored by an agency of the United States Government. Neither the United States Government nor any agency thereof, nor any of their employees, nor any of their contractors, subcontractors, or their employees, makes any warranty, express or implied, or assumes any legal liability or responsibility for the accuracy, completeness, or any third party's use or the results of such use of any information, apparatus, product, or process disclosed, or represents that its use would not infringe privately owned rights. Reference herein to any specific commercial product, process, or service by trade name, trademark, manufacturer, or otherwise, does not necessarily constitute or imply its endorsement, recommendation, or favoring by the United States Government or any agency thereof or its contractors or subcontractors. The views and opinions of authors expressed herein do not necessarily state or reflect those of the United States Government or any agency thereof.

Dynamically preferred state with strong electronic fluctuations from electrochemical synthesis of sodium manganate

Xi Chen¹, Yichao Wang¹, Yiping Wang², Rebecca L. Dally³, Kamila Wiaderek⁴, Tianyu Qiao¹, Jue Liu⁵, Enyuan Hu⁶, Kenneth Burch², Jeffrey W. Lynn³, and Xin Li^{1*†}

1. School of Engineering and Applied Sciences, Harvard University, Cambridge, MA 02138, USA

2. Department of Physics, Boston College, Boston, MA 02467, USA

3. NIST Center for Neutron Research, National Institute of Standards and Technology, Gaithersburg, MD 20899, USA

4. Advanced Photon Source, Argonne National Laboratory, Argonne, IL 60439, USA

5. Neutron Scattering Division, Oak Ridge National Laboratory, Oak Ridge, TN, 37831, USA

6. Chemistry Division, Brookhaven National laboratory, Upton, NY 11973, USA

*Corresponding author: lixin@seas.harvard.edu

†: Lead Contact: lixin@seas.harvard.edu

Summary

Electrochemical (de-)intercalation is a delicate method to precisely control the alkaline ion composition in alkaline transition metal oxides. Due to complicated interactions, metal charge ordering patterns can spontaneously form at special fractional alkaline compositions and orderings. Here we show that this elegant electrochemical process can create dynamically preferred structures in an anharmonic energy landscape that conventional syntheses and computations can rarely visit. Specifically, electrochemically prepared $\text{Na}_{1/2}\text{MnO}_2$ ordering exhibits abnormal structure distortions, charge orderings and dynamical activities. Strong magnetic fluctuations and lattice dynamics are observed in an unusually wide temperature range in $\text{Na}_{1/2}\text{MnO}_2$, which distinguishes it from all other Na_xMnO_2 at higher or lower Na compositions. The results emphasize the unique opportunity of using electrochemical processes to design and create novel quantum states with strongly coupled and mutually enhanced electronic and lattice fluctuations, likely through a special dynamic charge flux functional as suggested by our computational investigations.

Keywords: anharmonic phonon coupling, lattice and electron dynamics, charge flux fluctuations, strong magnetic fluctuations, sodium manganates, charge flux functional

Introduction

NaTMO_2 (TM = 3d transition metals) compounds have been widely studied as battery electrode materials.¹⁻³ Importantly, they also often provide unique prototypical materials where important quantum effects emerge from strong electronic correlations.⁴⁻⁸ In this article, we first identify the uniqueness of a $\text{Na}_{1/2}\text{MnO}_2$ ordered phase with abnormal Jahn-Teller (JT) distortions through a systematic structure analysis and

comparison of all the electrochemically prepared Na_xTMO_2 (TM = late 3d transition metals of Mn, Ni, Co, $0 < x \leq 1$), by (*in situ*) synchrotron X-ray diffraction (SXRD) and neutron diffraction measurements, combined with density functional theory (DFT) simulations. We then unveil the anomaly in temperature dependences of anharmonically coupled phonons in $\text{Na}_{1/2}\text{MnO}_2$ from base temperature to 300 K in Raman spectroscopy measurements and DFT simulations. A long-range magnetic ordering below the Néel temperature (T_N) at 47 K is also observed in neutron diffraction measurements, with the magnetic ordering consistent with DFT predictions, and with the T_N corresponding well to the temperature of Raman anomalies. A strong magnetic fluctuation above T_N emerges from the neutron order parameter analysis of $\text{Na}_{1/2}\text{MnO}_2$, which extends in an abnormally wider temperature range, compared with samples of Na_xMnO_2 at $x = 1, 5/8, 1/3$ obtained by the same synthesis method. Inelastic neutron scattering measurements show that the spin gap of $\text{Na}_{1/2}\text{MnO}_2$ closes above T_N , with strong magnetic fluctuations above the long-range ordered state due to short range magnetic correlations.^{8–12}

Our analysis suggests that there is an important interplay between structure instability and anharmonic stabilization in $\text{Na}_{1/2}\text{MnO}_2$ that provides and connects the observed vibrant electronic and lattice dynamics. Specifically, our DFT simulation unveils that there are strong dynamical charge transfers between ions, or charge fluxes, that are more confined in the $\text{Mn}^{3.5+}\text{O}_6$ charge stripe region (or simply the stripe region) of $\text{Na}_{1/2}\text{MnO}_2$ than other regions of the crystal. Here a higher level of “confinement” means that the charge flux happens more within the geometric space defined by the stripe region. More importantly, we find that these charge fluxes in $\text{Na}_{1/2}\text{MnO}_2$ much more effectively modulate the dynamical coupling of charge, lattice, and magnetic interactions than Na_xMnO_2 at other Na compositions. DFT simulations show that dominant magnetic exchange constants can be transiently modulated by strongly coupled anharmonic phonons through such charge fluxes, which suggests that both anharmonic phonon coupling and magnetic exchange could be functionals of the entire transient distribution of charge fluxes, in analogy to the more familiar construction of energies being considered as functionals of charge density distribution in DFT. The dynamic emergent phenomenon found in the model system of $\text{Na}_{1/2}\text{MnO}_2$ here thus provides a new perspective and

methodology, focused on the charge flux¹³ functional on top of the conventional charge density functional, to further understand other strongly correlated materials with amplified or new functionality often approaching structure instabilities, such as perovskite solar cell materials¹⁴ and nickelate and cuprate superconductors.^{15,16}

Results and Discussion

The late-3d transition metals can in principle show JT activity^{17,18} in the TMO_6 octahedron of layered Na_xTMO_2 , when the e_g orbitals are partially occupied, such as for Mn^{3+} and Ni^{3+} . Depending on if dx^2-y^2 or dz^2 orbitals are occupied, the octahedron can show compressed (4-long and 2-short Mn-O bonds) or elongated (2-long and 4-short) tetragonal local symmetry, also called negative or positive JT distortion modes, respectively. At $x = 1$, the synthesized Na_xTMO_2 compounds all show the O3 oxygen layer stacking (ABCABC stacking),¹⁹ which contains the fundamental configuration with the two elongated JT long-axes in positive Mn^{3+}O_6 or Ni^{3+}O_6 octahedron pointing directly toward Na ions. Strong Na-Mn-O orbital interactions were found in such a configuration, which manifest through the robustness of such or similar configurations identified in the ordering patterns of Na_xMnO_2 throughout the Na de-intercalation in a wide Na composition range of $1/18 \leq x \leq 1$, with the stacking being always kept at O3 at $1/3 \leq x \leq 1$.^{7,20} However, upon Na de-intercalation in the other late-3d Na_xTMO_2 that can reach a Na composition down to $x = 1/3$ (e.g., TM = Ni, Co), this Na-TM-O configuration has to be anyway modified significantly, as the oxygen stacking is changed to P3 (AABBCC)¹⁹ spontaneously at around $1/2 \leq x \leq 2/3$. The special O3- Na_xMnO_2 phase thus becomes the only late-3d $\text{Na}_{1/2}\text{TMO}_2$ that can show a stable O3 stacking near half Na composition in Na de-intercalation. Previous works studied the phase evolutions in these Na_xTMO_2 through either computations^{21,22} or experiments.^{7,20,23,24}

Here we first present a systematic comparison of the phase evolution in Na_xTMO_2 (TM = Mn, Ni, Co, $0 < x \leq 1$), determined by *in situ* SXR D refinements (Fig. 1a), where Na-ion battery was cycled for

electrochemical (de-)intercalation with continuous Na composition change in an *in situ* battery cell with X-ray transparent windows on both electrode sides, while SXRD patterns were taken simultaneously in the transmission mode to monitor the structure evolution. The refinements (SI Fig. 1-6) of the *in situ* SXRD patterns (SI Fig. 7-8) identify three major Na ordering phases for Na_xNiO_2 and Na_xCoO_2 at $x = 2/3, 1/2$ and $1/3$, while our previous reports identified orderings at $x=5/8, 1/2$ and $1/3$ for Na_xMnO_2 .^{7,20} The specific Na ordering patterns are shown in SI Fig. S9, together with their stackings. The phase diagram in Fig. 1a summarizes the information of Na_xNiO_2 , Na_xCoO_2 and Na_xMnO_2 , which is largely consistent with previous simulations for TM = Mn^{7,20,22} and Co²¹ and our own DFT simulations for TM = Ni (SI Fig. S10). Starting from the same O3 stacking at $x = 1$, the three materials, however, start to show very different orderings and stackings around $x = 2/3 \sim 5/8$, with TM = Mn keeping the O3 stacking while TM = Ni and Co showing a transformation to the P3 stacking instead. But at $x = 1/3$ all three materials merge into the same Na ordering and O3 stacking (SI Fig. S9). We want to emphasize again that the comparison unveils a unique property of Na_xMnO_2 to stay in the O3 phase and avoid the P3 phase in the entire phase evolution down to $x = 1/3$, including both Na orderings at $x = 1/2$ and $x = 1/3$, while Ni and Co systems show the P3 phase at $1/2 \leq x \leq 2/3$.

The focus of this paper is on the unusual state of O3- $\text{Na}_{1/2}\text{MnO}_2$ that exhibits abnormal JT distortions and charge ordering. Fig. 1b shows the structure evolution of main phases in Na_xMnO_2 upon electrochemical deintercalation of Na at $x = 5/8, 1/2$ and $1/3$. At $x = 1/2$, DFT simulations found multiple competitive states of δ^+ , and δ^- , v^- , v_0^- . The v_0^- phase is the DFT ground state, where the subscript “0” is for ground state, the superscript “-” is for negative JT distortion of Mn^{3+}O_6 octahedron as illustrated by red arrows, and “v” is for “normal” octahedral Na sites that all the Na ions occupy in the structure as illustrated by yellow balls. However, previous work²⁰ found that in $\text{Na}_{1/2}\text{MnO}_2$ there exists significant amount of the Na ions at the displaced Na site (Na_{disp}) that are shifted halfway between two normal sites along the *b* direction (SI Fig. S11a) with a different local environment than the normal Na site based on XRD refinements, very similar to the Na_{disp} sites first found in $\text{Na}_{5/8}\text{MnO}_2$.⁷ This detail suggests that the experimental structure of

$\text{Na}_{1/2}\text{MnO}_2$ should at least include the δ^+ or the δ^- states, where “ δ ” is for “displaced” Na sites (Na_{disp}) as illustrated by orange balls, while the superscripts “+” and “-” are for positive and negative JT distortions of Mn^{3+}O_6 , respectively.

We thus performed refinement of *in situ* SXRD at $x = 1/2$ on the lattice parameters, with internal coordinates fixed at those from the DFT δ^+ , δ^- , v^- and v_0^- states, and obtained goodness-of-fit R_{wp} of 5.089, 4.849, 4.941, and 4.920, respectively (See Methods and SI Fig. S11b,c,d for more information). These numbers are relatively close to the $R_{wp} = 3.51^{19}$ from the full refinement including both the lattice parameters and internal coordinates. Furthermore, the refinement difference among these states is actually small, although δ^- is slightly better than others. Since structural evolution from one state to another among the four structures just needs some local Na shift along the b direction together with the local charge transfer between Mn ions, as can be easily seen from Fig. 1b, the SXRD refinement results here cannot inarguably distinguish δ^+ from δ^- , or exclude the possibility of their coexistence with v^- or v_0^- . We will thus present neutron diffraction, including the measured magnetic ordering, and neutron pair-distribution-function (nPDF) results later to demonstrate the preference to δ^- over δ^+ , as well as the electronic and magnetic fluctuation results from the band and lattice dynamics in DFT simulations and the temperature evolution of neutron diffractions to emphasize the importance of the δ^- state over the other three states.

However, here we want to first provide some evidence favoring the δ^- state based mainly on a more detailed comparison of DFT simulations with *in situ* SXRD refinements, to make the readers more familiar with these structures. Fig. 1c shows that approaching experimental lattice parameters, δ^- becomes energetically competitive, not only in absolute energy values, but more importantly, showing a local energy minimum that δ^+ lacks. The DFT δ^- state exhibits the anomaly of weakly compressed $\text{Mn}^{3.5+}\text{O}_6$ octahedron (δ^- -Mn2 in Fig. 1c) with actually comparable lengths in the six Mn-O bonds, and obvious $\text{Mn}^{3.5+}$ dimerization along the pure $\text{Mn}^{3.5+}$ charge stripe in the b direction (pink stripe in Fig. 1b). The neighboring

$\text{Mn}^{3+/4+}$ b stripes (stripe with mixed purple and grey hexagons in Fig. 1b) show strongly compressed Mn^{3+}O_6 (δ^- -Mn1 in Fig. 1c) with negative JT distortions. δ^+ on the contrary exhibits only Mn^{3+}O_6 with strong positive JT distortions. Note that the lattice parameters a , b , c , including β , of the δ^- state are very close between experimental and DFT fully relaxed ones, while that of the δ^+ state are not (SI Fig. S11c). We thus evolve total energies in DFT simulations from the δ^- state at experimental lattice parameters that are nearly equivalent to DFT relaxed ones to δ^+ with a very different DFT relaxed lattice parameters (Fig. 1d), which shows a small local barrier to overcome.

The δ^- state also shows the highest structure correlation in Fig. 1e to the structure from our SXRD refinement of electrochemically prepared $\text{Na}_{1/2}\text{MnO}_2$,²⁰ due to the structure details of Mn dimerization, the bond length and angle in the special distortions of MnO_6 octahedra, and the spatial distribution of these octahedra. The refined structure of $\text{Na}_{1/2}\text{MnO}_2$ is shown in Fig. 2ab, while the four DFT structures of ν_0^- , ν^- , δ^+ , and δ^- at $x = 1/2$ are shown in SI Fig. S11. However, it is worth noting that contrary to $\text{Na}_{5/8}\text{MnO}_2$ ⁷ and the δ^+ state at $x = 1/2$ ²⁰ where Na_{disp} is at the local minima, Na_{disp} in δ^- indeed stays at the saddle point, suggesting that the existence of δ^- in experiment may rely on certain dynamical effects.¹⁴ In addition, for Na_xMnO_2 at both $x = 5/8$ and $1/3$ orderings, we have confirmed that no such complexity from competing states in DFT exists. The ground state structures from DFT simulations at $x = 5/8$ and $1/3$ are fully consistent with SXRD refinements^{7,20} and all show strongly elongated positive JT distortions (Fig. 1b, SI Fig. S12).

The DFT δ^- state at $x = 1/2$ shows unique static electronic structures (Fig. 2c), as well as the dynamic ones under ionic perturbations, compared with other states at $x = 1$, $5/8$, $1/2$, and $1/3$ (Fig. 2d, SI Fig. S13). The δ^- state is the only structure with the top band passing through the Fermi level (E_f), and hence with a partial occupancy for a more collective behavior of charge carriers ($\Delta E_1 = 0$). The band is from pd hybridization of the unique weakly compressed $\text{Mn}^{3.5+}\text{O}_6$, which is well separated from bottom bands ($\Delta E_2 = 0.2 \sim 0.4$ eV), suggesting little intermixing with other bands. The band also shows a reasonably wide band width (W

= 0.42 eV), indicating that electrons will not be strongly localized. At $x = 1/3$, W is much narrower with much larger ΔE_1 and ΔE_2 , suggesting strong electron localization; while at $x = 1$ and $5/8$, W is much wider with ΔE_2 almost closed, suggesting strong delocalization and band intermixing (See blue original lines in Fig. 2d and more details in SI Fig. S13). The results are consistent with density of states (DOS) analysis (SI Fig. S14).

Furthermore, we find that for the structures at $x = 1, 5/8$ and $1/2$ (δ^+) with clear Mn^{3+} stripes (purple straight stripes along b direction in Fig. 1b), ionic perturbations in DFT tend to generate a large change of W , while for structures as $x = 1/3$, ΔE_1 and ΔE_2 are more sensitive to such perturbations. The electronic structure of δ^- state at $x = 1/2$ is, however, relatively robust against ionic perturbations. These trends are clearly illustrated in Fig. 1d by the red and grey curves for W , ΔE_1 and ΔE_2 being perturbed by elongating or shortening a pair of oxygens in the Mn-O bonds corresponding to the elongated JT direction (labelled as O_{JT} hereafter) along the (101) plane (blue plane in Fig. 2a).

Consistent with the above static band structure and band dynamics in reciprocal space, strong couplings of charge fluxes and lattice dynamics in real space are found in the δ^- state. When perturbing a pair of O_{JT} along the (101) plane, or perturbing a $\text{Mn}^{3.5+}$ in the pair of $\text{Mn}^{3.5+}$ dimers along the b direction --- which are the critical components of the two important phonon modes to be discussed later --- charge fluxes (f) are generated, as illustrated in Fig. 2e, which can be analyzed from the charge density difference results (SI Fig. S15). Since later it will be shown that abnormal magnetic fluctuations are likely to be strongly correlated with such fluxes in the $\text{Mn}^{3.5+}\text{O}_6$ stripe region generated from these phonons, we now focus on analyzing the strength of fluxes inside (f_i) and outside (f_o) the stripe region due to different ion perturbations, as well as the flux confinement ratio $f_i/(f_i + f_o)$ of the stripe region (See Methods). We find that under both perturbations in Fig. 2e, strong fluxes are generated within the $\text{Mn}^{3.5+}$ stripe region (pink stripe in Fig. 1b and Fig. 2e), while a small portion of charge flows to the neighboring $\text{Mn}^{3.5+}$ stripe, or leaks to the $\text{Mn}^{3+/4+}$ stripe (stripe with mixed purple and grey hexagons).

We then extend the above flux analysis based on the perturbation of a single ion or a pair of ions to the perturbations from the entire phonon spectra for all these structures in Fig. 2f, 2g. Flux strength is thus analyzed within the entire $\text{Mn}^{3.5+}$ stripe region formed by all the parallel pink stripes in a supercell (Fig. 2e), generated by each phonon mode as shown by an individual grey dot in Fig. 2f. The flux confinement ratio is also calculated in the same way based on fluxes within the entire $\text{Mn}^{3.5+}$ stripe region (i.e., f_i) or not (i.e., f_o), as shown in Fig. 2g. We find that δ^- not only shows the strongest average fluxes (Fig. 2f), but also shows relatively high flux confinement ability of the stripe region (Fig. 2g). This could be caused by the partially occupied non-narrow band near E_f that is also well-separated from other bands, with the features also robust against ionic perturbation (Fig. 2cd). The partial occupancy and certain band width support a more collective and robust electron motion in response to phonons, while the separation from other bands prevents intermixing of electrons to other bands so that fluxes can be better confined in the top band that resides mainly in the $\text{Mn}^{3.5+}$ stripe region. This describes a unique picture of strong collective fluxes that are spatially confined in the $\text{Mn}^{3.5+}$ stripe region of the δ^- state at $x = 1/2$.

To further understand the influence of the unique band and flux dynamics of the δ^- state to the lattice dynamics and (dynamic) magnetic properties, we perform chemical desodiation from NaMnO_2 to create clean and sufficient powder sample of $\text{Na}_{1/2}\text{MnO}_2$ that is needed for Raman and neutron measurements. The NaMnO_2 sample was synthesized and sintered in exactly the same way as the one used for electrochemical desodiation in the *in situ* SXRD measurement. The chemical desodiation of the powder sample was made by soaking NaMnO_2 in the solution of iodine (see Methods), which is one of the gentlest oxidizers, for much longer time than we performed the electrochemical desodiation to reach $\text{Na}_{1/2}\text{MnO}_2$. These approaches are to minimize any defects by chemical desodiation. SXRD measurement of the chemically desodiated $\text{Na}_{1/2}\text{MnO}_2$ powder shows a great match in structural details to the *in-situ* SXRD pattern of Na_xMnO_2 at $x = 1/2$ (SI Fig. S16).

Figure 3a shows the Raman spectra of electrochemically prepared $\text{Na}_{1/2}\text{MnO}_2$ cooling from room temperature to 10 K. Large frequency shifts with temperature are mainly observed for peaks at low and high frequencies, such as at 125 cm^{-1} and 400 cm^{-1} (SI Fig. S 17). The Raman peak shifts of the 16 clearly observable modes are shown in Fig. 3b, with the effect of thermal expansion subtracted (See Methods). Many modes at $< 130\text{ cm}^{-1}$ and $> 300\text{ cm}^{-1}$ show strong peak shifts, suggesting a strong anomalous anharmonicity. Figure 3c presents the anharmonic phonon coupling strength G in DFT simulations between each pair of the 37 modes in the phonon spectrum of δ^- state (See Methods). By comparing the experimental Raman spectra with the calculated phonon density of states (SI Fig. S18, S19), we find that strong couplings exist among a subset of modes in δ^- , including the four lowest frequency modes # 0-3 ($< 130\text{ cm}^{-1}$) with the strongest Na movements, and the higher frequency modes # 13, 17, 22, 25, 28, 30 and 32 ($> 300\text{ cm}^{-1}$) with majority Mn and O ion movements. Compared with all other structures (Fig. 3d, SI Fig. S20), the δ^- state also shows the strongest coupling strength G that is outstanding among Na_xMnO_2 , where the ground energy state v_0^- at $x = 1/2$ is actually one of the weakest. This also suggests that δ^- - $\text{Na}_{1/2}\text{MnO}_2$ is preferred by anharmonic stabilization. Softening of the anharmonic phonon couplings here, on the other hand, is also likely to decorate δ^- with subtle additional distortions.^{14,25,26}

Temperature dependent neutron diffraction of $\text{Na}_{1/2}\text{MnO}_2$ (Fig. 4ab, SI Fig. S21 and S22) shows a long-range magnetic ordering phase transition temperature T_N at 47 K. The magnetic peaks measured by neutron diffraction below T_N match the model shown in the inset of Fig. 4a from neutron refinements. The refined magnetic structure is an antiferromagnet with ordering wavevector $\mathbf{k} (r.l.u.) = (0, 0, 1/2)$. The magnetic peaks from here on are referenced with respect to the magnetic unit cell, which is doubled along the c -axis with respect to the nuclear unit cell. This magnetic ordering is also predicted by magnetic coupling constants J from DFT simulations as the ground state magnetic structure of δ^- state (SI Fig. S23). The $J_{33}^{(1)}$ along the b stripe direction between two nearest $\text{Mn}^{3.5+}$ ions shows the strongest ferromagnetic (FM) coupling that dominates the FM b stripe ordering, where the superscript (1) represents the nearest neighbor Mn-Mn

interaction, while 3 in the subscript represents the valence of Mn (which is just a notion and should not be taken as exact here as the valence suggested by DFT is around 3.5+). The abnormal JT distortions of weakly compressed $\text{Mn}^{3.5+}\text{O}_6$ in the δ^- state (Fig. 1c, SI Fig. S11) may cause the FM coupling of $J_{33}^{(1)}$, while $\text{Na}_{5/8}\text{MnO}_2$ ⁷ and the δ^+ state at $x = 1/2$ with strongly elongated JT distortions instead prefer antiferromagnetic (AFM) $J_{33}^{(1)}$ couplings along similar stripe patterns in our DFT simulations. The δ^+ state thus gives a very different magnetic structure from DFT prediction that cannot be refined by the neutron diffraction data. Therefore, the magnetic structure from neutron diffraction measurement of $\text{Na}_{1/2}\text{MnO}_2$ at low temperature below T_N provides strong evidence to include the δ^- state while simultaneously help exclude the δ^+ state. In addition, the neutron diffraction and neutron PDF measurements at room temperature also show obviously better refinement goodness-of-fit for δ^- with $R_{\text{wp}} = 11.1\%$ (diffraction) and 15.9% (PDF), compared with the 14.0% and 17.9%, respectively, of δ^+ (SI Fig. S24).

The transition temperature T_N obtained from fitting the intensity of the (10-1) magnetic peak versus temperature matches well with the inflection point in the inverse SQUID susceptibility (Fig. 4b). The inset shows that near T_N , the weighted average peak position has a sudden shift toward higher angle, and the magnon gap measured by inelastic neutron scattering disappears (SI Fig. S25). Above T_N , however, significant neutron intensity remains and decreases slowly with temperature, indicating strong magnetic fluctuations above the magnetic long range ordered state, in a very wide temperature range. In comparison, such remaining neutron intensity of Na_xMnO_2 at other Na compositions decays quickly above T_N (Fig. 4c).^{7,10,11,20} The integrated residue intensities from T_N to high temperatures highlight the anomaly of $\text{Na}_{1/2}\text{MnO}_2$ (Fig. 4c inset), which is about 3 times larger than NaMnO_2 with well-known spin fluctuations due to low dimensionality or geometric frustration,⁹⁻¹² and more than 7 times larger than $\text{Na}_{5/8}\text{MnO}_2$ with a similar 1D stripe pattern (Fig. 1b). Note that especially for $x = 1/3$ ²⁰ and $x = 5/8$ ⁷ the Na_xMnO_2 powder was synthesized and chemically desodiated in exactly the same way by us as $x = 1/2$, and the neutron diffraction were performed by the same instrument and measurement configuration. Therefore, we believe the unique strong

magnetic fluctuation observed in $\text{Na}_{1/2}\text{MnO}_2$ reflects certain intrinsic changes from other Na compositions, rather than being caused by trivial factors such as defects generated in synthesis.

Raman measurements of $\text{Na}_{1/2}\text{MnO}_2$ further reveal anomalies around T_N , suggesting a strong magnon-phonon coupling. For some Na modes at low frequencies, the Raman susceptibility quickly increases with decreasing temperature below T_N , while the change is noticeably slower above T_N (Fig. 4d). For other high frequency modes, an opposite trend is observed. For the Raman peak full-width-half-maximum (FWHM) versus temperature, the Na modes all have a bump around 50-70 K, while such an anomaly cannot be found in other modes (Fig. 4e). DFT simulations further show that dynamically the value of $J_{33}^{(1)}$ is very susceptible to, and also strongly coupled to phonon oscillations in the δ^- state. We first use two strongly coupled modes as an example to illustrate this effect before the demonstration using the entire phonon spectrum. With increasing phonon amplitude of the dimer mode (#22) or O_{IT} mode (#25), as illustrated in SI Fig. S26a, the $J_{33}^{(1)}$ changes from FM toward AFM couplings, with the general trend proportional to the phonon induced difference in magnetic moments between the two neighboring $\text{Mn}^{3.5+}$ ions in the stripe region. The strong anharmonic phonon coupling between the two modes further leads to faster change of $J_{33}^{(1)}$ to become AFM (black dots in SI Fig. S26b), just above the zero-point amplitude. Note that our phonon simulations show that at around T_N (47K), the average ion oscillation amplitude already reaches 1.5 times that at 0 K (SI Fig. S27). Thus, strongly coupled phonons in the δ^- state exhibit the ability to fluctuate the dominant magnetic exchanges between FM and AFM couplings above T_N .

Such DFT simulations are then extended to all possible phonon pairs. We rank the relative change of magnetic coupling constants, $\Delta J/J_0$, caused by all phonon mode pairs of each Na_xMnO_2 structure, and present their converged mean top values in Fig. 4f. We then calculate the correlation of this $\Delta J/J_0$ rank with the previous G rank (Fig. 3d and inset) for each structure, which is an indicator about how likely a strongly coupled phonon pair will also generate a strong change of magnetic coupling in any Na_xMnO_2 structure

(Fig. 4g), where an extra 10% in both ranks is included for the accuracy of the correlation calculation. Finally, the most relevant metric of $\Delta J/J_0 \cdot G$ to the electronic dynamics in Na_xMnO_2 is presented in Fig. 4h, which shows that the effect of coupled lattice and magnetic dynamics is indeed the most magnificent in the δ^- state compared with other Na_xMnO_2 states, matching well with the trend of magnetic fluctuation strength along $x = 1, 5/8, 1/2, 1/3$ in the neutron analysis in Fig. 4c inset. Note that although NaMnO_2 shows a relatively strong G (Fig. 3d inset), it lacks the correlation with $\Delta J/J_0$ (Fig. 4g); while $\text{Na}_{1/3}\text{MnO}_2$ does show both a large $\Delta J/J_0$ and a high correlation to G , its phonon coupling strength G , however, is too low (Fig. 3d inset). Therefore, the metric that calculates $\sum_i \Delta J_i/J_0 \cdot G_i$ here actually requires both to be strong and happen simultaneously, which is only found in the thermodynamically unstable δ^- - $\text{Na}_{1/2}\text{MnO}_2$ state that is however preferred by anharmonic stabilization in experiment.

The above analysis thus also emphasizes the importance of the δ^- state than other states of v_0^- , v^- and δ^+ at $x = 1/2$ in contributing to the strong magnetic fluctuation observed in neutron order parameter analysis of $\text{Na}_{1/2}\text{MnO}_2$. Compared with δ^- , the v_0^- , v^- and δ^+ states can also be considered as silent states in terms of magnetic fluctuations (Fig. 4h). However, it is worth noting that although the δ^+ state has been largely excluded by the magnetic long-range ordering structure analysis, together with the worse neutron diffraction and neutron PDF refinement compared with the δ^- , the remaining two states of v_0^- and v^- at $x = 1/2$ cannot be fully excluded. They show similar SXRD (SI Fig. S11) and neutron diffraction (SI Fig. S28) refinement results to the δ^- state. Also, their magnetic couplings along b direction are FM as well, which is the same as δ^- , so the magnetic ordering structure suggested by neutron magnetic diffraction refinement cannot exclude v_0^- and v^- either. Considering that they are silent in magnetic fluctuation and v_0^- is actually the DFT ground energy state, including them together with the δ^- state in $\text{Na}_{1/2}\text{MnO}_2$ will not violate known experimental facts here. That said, the opposite is not true, that is, excluding the δ^- state will lose the flux, magnetic and lattice dynamics that are unique to δ^- and required by the synergy between our experimental and computational data. We thus also performed two-phase refinements of $\text{Na}_{1/2}\text{MnO}_2$

neutron diffraction data for $\delta^- + v_0^-$ and $\delta^- + v^-$, which shows an improved goodness-of-fit for R_{wp} from around 11% for δ^- , v_0^- or v^- individual phase to around 7.5% for the two-phase (SI Fig. S28). This suggests that the possibility of two-phase coexistence, or an even larger supercell that orders alternating regions representing the two phases, should not be excluded.

Specifically, if we go beyond the primitive cell size defined by the four DFT low-energy states, a larger supercell with alternating δ^- and v_0^- or v^- regions can be constructed. This approach is actually important to enabling the superstructure XRD to match the small XRD peak at 4.7-degree (SI Fig. S16), which does not correspond to any set of (hkl) planes in the primitive cell of the four low-energy states of v_0^- , v^- , δ^- , and δ^+ . Our crystallographic analysis shows that it requires a supercell with at least doubled primitive cell size in the b direction. For example, in a supercell with four times in a direction and two times in b direction (SI Fig. S29), our DFT simulation shows that the δ^- type and the mixed v^-/v_0^- type block regions alternating along the a direction can coexist, where the dynamically important $Mn^{3.5+}$ stripe in the δ^- state can be maintained in periodic block regions. Note that such unusually large supercell is not uncommon in the Na_xMnO_2 system, as what has been found before in $Na_{5/8}MnO_2$.⁷ This $Na_{1/2}MnO_2$ structure illustrated in SI Fig. S29, together with many other structures with such combinations of δ^- , v^- , and v_0^- block regions that we checked, all can fit this 4.7-degree peak, with one example being shown in SI Fig. S30 for the comparison between XRD simulations, refinements, and experiments. Although further resolving the exact large supercell structure that combines the several DFT low-energy states for $Na_{1/2}MnO_2$ could be complicated and requires more advanced characterizations and computations, the analysis here, nevertheless, emphasized the inclusion of the dynamically preferred δ^- state region, as the main focus of this paper.

Conclusion

In conclusion, the strong collective flux confined inside the $\text{Mn}^{3.5+}\text{O}_6$ stripe region unique to δ^- - $\text{Na}_{1/2}\text{MnO}_2$ is likely to play a critical role here. Such directional fluxes originated from the collective dynamics of electrons and lattices, i.e., f^d , may effectively transfer the energy of anharmonic phonon coupling G to transiently modulate the magnitude or even flip the sign of dominant magnetic coupling constants J , i.e., causing a big ΔJ in a wide temperature range above T_N , with G and ΔJ simultaneously controlled by f^d . This results in certain nontrivial functional relationships of $\Delta J(f^d)$ and $G(f^d)$, interacting mainly through the entire transient distribution of the f^d function in the crystal. This emphasizes the physical significance of the dynamic charge flux functionals over the static charge density functionals to such a dynamically preferred state created by electrochemical processes. Our picture will impact the understanding of the relationship between strong electronic fluctuations, functionalities and structure instabilities, making it potentially relevant to other novel quantum states, where high conversion efficiency is often found in those perovskite solar cell materials at metastable and unstable states,¹⁴ and novel superconducting related properties can emerge from nickelates near such structure instability from electrochemical synthesis.¹⁵

Experimental procedures

Resource Availability

Lead Contact: Xin Li, e-mail (lixin@seas.harvard.edu)

Materials Availability

This study does not generate new unique materials. For synthesis of Na_xMnO_2 , please refer to the Synthesis section.

Data and Code Availability

The datasets generated during the current study are available from the corresponding author upon reasonable request.

The code to analyze the data is available from the corresponding author upon reasonable request.

Synthesis

Pristine NaMnO_2 , NaNiO_2 and NaCoO_2 powder was synthesized by solid-state reactions, following previous publications^{19,27,28}. The $\text{Na}_{1/2}\text{MnO}_2$ powder for the neutron diffraction and PDF measurement was obtained by chemical de-intercalation of pristine NaMnO_2 powder in an iodine acetonitrile solution with a 3:1 molar ratio of iodine over Na, reacted for 24 hours at room temperature inside a glove box. The chemically desodiated $\text{Na}_{1/2}\text{MnO}_2$ was confirmed to be free from impurity phase or structure disorder by matching its SXRD profile with the profile of $\text{Na}_{1/2}\text{MnO}_2$ from *in-situ* SXRD (SI Fig. S16). The cathode film of $\text{Na}_{1/2}\text{MnO}_2$ for Raman measurement was obtained by electrochemical method²⁷ with a C/50 charging rate until reaching the ~3.0V plateau, which corresponds to the strongest $\text{Na}_{1/2}\text{MnO}_2$ ordering recorded in *in-situ* XRD.

(*In-situ*) synchrotron XRD

In situ SXRD experiments were performed at the powder diffraction beamline, 11-BM, at the Advanced Photon Source at Argonne National Laboratory. High angular resolution X-ray diffraction data were collected using a 12-channel analyzer detector array ($\lambda = 0.413609 \text{ \AA}$, beam size $1.5 \times 0.5 \text{ mm}$). Data spanning a 0° – 26° 2θ range were collected using a step size of 0.002° . Measurements were taken at C/50 rate²⁰ on every 2 h interval with 30 min scanning time for each pattern, corresponding to 4% Na composition interval between patterns and 1% Na composition resolution per pattern. Ex situ synchrotron XRD measurement on chemically desodiated $\text{Na}_{1/2}\text{MnO}_2$ were performed in a sealed capillary and collected at beamline 28-ID-2 of the National Synchrotron Light Source II at Brookhaven National Laboratory, using a photon wavelength of 0.1844 \AA . An amorphous silicon flat panel two-dimensional detector (Perkin Elmer) was used and the raw image data was radially integrated using Fit2D software. The beam size used in this work was $1 \times 1 \text{ mm}$. Rietveld refinements were performed within the Topas software. The backgrounds of XRD patterns are approximated by Chebyshev polynomials of order 30.

Neutron diffraction, neutron PDF and magnetic susceptibility

Neutron diffraction measurements were performed on 5 g of chemically deintercalated $\text{Na}_{1/2}\text{MnO}_2$ powder using the triple-axis spectrometer BT-7²⁹ at the NIST Center for Neutron Research. A closed cycle He refrigerator with a base temperature of 2.5 K was employed, using a wavelength of 2.359 Å and a position sensitive detector. Inelastic measurements to determine the spin gap were taken on the SPINS cold neutron spectrometer with a fixed final energy of 5 meV. Heatmap neutron measurements were swept at 10 K/min within each 5 K temperature step, with each measurement of 5min at a given temperature, giving around 6 hours of total measurement time from 300 K to 2.5 K. The calculation of the intensity of the neutron scattering uses the formula $|F(hkl)|^2/(\sin \theta \sin 2\theta)$, where F is the structure factor of the product of collinear spin and a phase factor $\exp(-2\pi i(hx + ky + lz))$, and (x, y, z) is the coordinate of each Mn ion. 2θ is the scattering angle. The magnetic susceptibility measurements were obtained using a Quantum Design MPMS-3 SQUID at 20 Oe in DC mode (note: 1 Oe = 1000/4π A/m), with a sweeping rate of 4 K/min within each 2 K temperature step, giving around 5 hours of total measurement time for a ZFC or FC between 300 K and 1.8 K.

The chemically deintercalated $\text{Na}_{1/2}\text{MnO}_2$ powder was also sealed in capillaries for neutron diffraction and nPDF measurements at room temperature at NOMAD beamline at the Spallation Neutron Source, Oak Ridge National Laboratory. The one of the fastest neutron diffractometers in the world,^{30,31} high neutron flux and large detector enables the usage of only 0.3 g powder sample, which was loaded into thin-walled quartz capillary (diameter of 3mm). Four 24 min scans were collected and summed together to improve the statistics. Signal from empty quartz capillary was subtracted, with the obtained intensity being normalized to correct for the detector efficiency, and the absorption and multiple scattering being corrected. For the reduction of nPDF data, the inelasticity polynomial correction of the self-scattering was performed. The normalized distinct scattering function (SQ-1) was Fourier transformed to obtain the reduced PDF $G(r)$ with a Q_{max} cut-off of 35 Å⁻¹. The neutron diffraction structure refinements were carried out using Topas v6 software. Time-of-flight (TOF) were converted to d-spacing using a conventional 2nd order polynomial. For the low-resolution frames (bank 2 and 3), a back-to-back exponential function convoluted with a

symmetrical Gaussian function was used to describe the peak profile. For the high-resolution frames (bank 4 and 5), the moderator induced line profile was modeled using a modified Ikeda-Carpenter-David function.³²⁻³⁴ Lorentz polarization is corrected by multiplying d^4 . For nPDF analysis, the instrument constants Q_{broad} and Q_{damp} were determined from the refinement of a Si standard to be 0.19 \AA^{-1} and 0.21 \AA^{-1} , respectively.

Raman measurement

The Raman measurement was performed using an airtight sample holder with electrochemically prepared $\text{Na}_{1/2}\text{MnO}_2$ cathode film loaded inside an Ar filled glovebox before transferring to the Raman spectrometer.³⁵ To avoid damage and overheating artifact, the presented data using a laser power of $15 \mu\text{W}$ were double checked with the data at $5 \mu\text{W}$. 5 K/min temperature sweeping rate was used to reach a neighboring temperature, and $\sim 1.5 \text{ K/min}$ was used to reach the actual temperature. It takes an extra less than 5 minutes to reach near equilibrium before the first measurement at each temperature. Three Raman scans at each temperature were measured to make sure no drifting of laser spot was observed in the last two scans to guarantee the temperature stability in the reported 3rd scans in Fig. 3a. Each Raman spectrum measurement takes 20 min. The entire cooling measurement from 300 K to 10 K took around 25.5 hours. In Fig. 3c, an estimated volume thermal expansion coefficient of 10^{-5} K^{-1} ³⁶ is used. The Gruneisen parameter is 1.0 according to our DFT calculation. Raman susceptibility³⁷ is calculated from $\chi_R(T)/\chi_R(10 \text{ K})$, where $\chi_R(T) = I/(n_B + 1)$, with $n_B = \exp(-\hbar\omega/k_B T)$ as the Bose factor and I as the intensity of Raman peak.

DFT

All DFT calculations in this work were performed using the Vienna ab initio Simulation Package (VASP) within the projector augmented wave (PAW) approach using the Perdew-Burke-Ernzerhof GGA functional and the GGA+U extension to it. The U value for Mn is 3.9 eV, in line with previous literatures.²⁰ A 520 eV plane-wave energy cutoff was used for all calculations. The Brillouin zone was sampled using -centered Monkhorst-Pack meshes with a density of at least 28 \AA along each reciprocal lattice vector. Forces were

converged within to 0.01 eV/Å. The ground state structure and energy of each stacking phase at each Na composition in the NaNiO₂ phase diagram (Fig. S10) was obtained by DFT relaxation of the 30 Na orderings with the lowest Ewald energies. The lattice parameters were fully relaxed and the DFT-D3BJ van der Waals correction is employed. The number of oxygen ions in Mn³⁺O₆ is proportional for x=1/2 and x=5/8 but not for x=1/3, since in x=1/3 there is no edge-sharing between Mn³⁺O₆. In order to normalize, the flux contribution from oxygen in x=1/3 is scaled by a factor of 2/3 to make it proportional to the other cases. In the charge flux calculation, the direction of the flux is determined using the information of the total charge difference and charge distribution change of each ion, as well as local symmetry constraints. The Mn³⁺O₆ octahedra are defined as in-stripe, and other ions are defined as out-of-stripe. Charge confinement ratio was thus calculated based on the charge of ions obtained by integrating the site-decomposed DOS over the group of bands below the Fermi level, as described in Figure S13. The calculation of magnetic coupling and ground state was based on an Ising-like model, where the total energy is $E = -\sum_{\langle i,j \rangle} J_{ij} \sigma_i \sigma_j$ with all the possible J_{ij} up to the third nearest neighbor. σ_i takes value of ± 1 , corresponding to the “spin-up” and “spin-down” states. Phonon calculations were performed with enlarged supercells containing at least 32 formula units of Na_xMnO₂ with at least 10 Å in each lattice dimension. For example, the calculation for Na_{1/2}MnO₂ uses a supercell of 2*2*2=8 copies of the monoclinic unit cell of the Na_{1/2}MnO₂, which has 4 formula units of Na_{1/2}MnO₂ (Fig. 2a). The anharmonic phonon coupling calculation follows the previous method.^{13,38} The phonon calculations were performed in the framework of the Phonopy software.³⁹

Acknowledgements

This work was supported by Dean’s competitive fund of promising scholarship at FAS at Harvard University, and Harvard Data Science Initiative Competitive Research Award. Y.W. and K.S.B. acknowledge the primary support of the US Department of Energy (DOE), Office of Science, Office of Basic Energy Sciences under award no. DE-SC0018675. Computations were supported by computational

resources from the Texas Advanced Computing Center (TACC) and the Odyssey cluster supported by the FAS Division of Science, Research Computing Group at Harvard University. This work also made use of the Shared Experimental Facilities supported in part by the Materials Research Science and Engineering Centers (MRSEC) Program of the National Science Foundation under award no. DMR-1419807. Use of the Advanced Photon Source at Argonne National Laboratory was supported by the U. S. DOE, Office of Science, Office of Basic Energy Sciences, under Contract No. DE-AC02-06CH11357. The identification of any commercial product or trade name does not imply endorsement or recommendation by the National Institute of Standards and Technology. The work done at BNL is supported by the Assistant Secretary for Energy Efficiency and Renewable Energy, Vehicle Technology Office of the DOE through the Advanced Battery Materials Research (BMR) Program under contract no. DE-SC0012704. This research used beamline 28-ID-2 of the NSLS II, a US DOE Office of Science user facility operated for the DOE Office of Science by BNL under contract no. DE-SC0012704. The neutron diffraction studies at NOMAD used resources at the Spallation Neutron Source, a DOE Office of Science User Facility operated by ORNL.

Author Contribution

X. L conceived the project and planned the research. X.C performed the DFT calculations. Yichao. W synthesized NaMnO_2 , NaCoO_2 and NaNiO_2 powder samples for in situ SXRD and prepared the chemically desodiated $\text{Na}_{1/2}\text{MnO}_2$ for neutron and Raman measurements. Yiping. W and K.B performed Raman setup and measurement, with Yichao. W and X. C assisted the remote monitoring during the measurement. R. L. D and J. W. L performed the temperature dependent neutron diffraction and inelastic neutron scattering measurement, analyzed inelastic neutron scattering data and performed the magnetic structure refinement. X. L and K. W performed the *in-situ* synchrotron XRD measurement. T. Q obtained the phonon modes, DOS and temperature-dependent oscillation amplitudes from DFT calculations. Jue. L performed the neutron diffraction and neutron PDF measurement at room temperature and performed the structural

refinements. E. H performed the *ex-situ* synchrotron XRD measurement. X. C and X. L analyzed the experimental data with the help of discussions with all authors. X. C and X. L analyzed the computational and experimental results and wrote the manuscript. X.L conceived the physical picture of entangled magnetic and lattice dynamics through charge flux functionals.

Declaration of Interests

The authors declare no competing interests.

References:

1. Yabuuchi, N., Kubota, K., Dahbi, M., and Komaba, S. (2014). Research development on sodium-ion batteries. *Chem. Rev.* **114**, 11636–11682.
2. Ortiz-Vitoriano, N., Drewett, N. E., Gonzalo, E., and Rojo, T. (2017). High performance manganese-based layered oxide cathodes: overcoming the challenges of sodium ion batteries. *Energy Environ. Sci.* **10**, 1051–1074.
3. Delmas, C., Carlier, D., and Guignard, M. (2021). The Layered oxides in lithium and sodium-ion batteries: A Solid-State Chemistry Approach. *Adv. Energy Mater.* **11**, 2001201.
4. Guignard, M., Didier, C., Darriet, J., Bordet, P., Elkaïm, E., and Delmas, C. (2013). P2- Na_xVO_2 system as electrodes for batteries and electron-correlated materials. *Nat. Mater.* **12**, 74–80.
5. Roger, M. *et al.* (2007). Patterning of sodium ions and the control of electrons in sodium cobaltate. *Nature* **445**, 631–634.
6. Takada, K. Sakurai, H., Takayama-Muromachi, E., Izumi, F., Dilanian, R. A., and Sasaki.,

- T. (2003). Superconductivity in two-dimensional CoO_2 layers. *Nature* **422**, 53–55.
7. Li, X. *et al.* (2014). Direct visualization of the Jahn-Teller effect coupled to Na ordering in $\text{Na}_{5/8}\text{MnO}_2$. *Nat. Mater.* **13**, 586–92.
 8. Chen, X., Tang, H., Wang, Y., and Li, X. (2021). Balancing orbital effects and on-site Coulomb repulsion through Na modulations in Na_xVO_2 . *Phys. Rev. Mater.* **5**, 084402.
 9. Stock, C., Chapon, L. C., Adamopoulos, O., Lappas, A., Giot, M., Taylor, J. W., Green, M. A., Brown, C. M., and Radaelli, P. G. (2009). One-dimensional magnetic fluctuations in the spin-2 triangular lattice α - NaMnO_2 . *Phys. Rev. Lett.* **103**, 077202.
 10. Dally, R. L., Chisnell, R., Harriger, L., Liu, Y., Lynn, J. W., and Wilson, S. D. (2018). Thermal evolution of quasi-one-dimensional spin correlations within the anisotropic triangular lattice of α - NaMnO_2 . *Phys. Rev. B* **98**, 144444.
 11. Giot, M., Chapon, L. C., Androulakis, J., Green, M. A., Radaelli, P. G., and Lappas, A. (2007). Magnetoelastic coupling and symmetry breaking in the frustrated antiferromagnet α - NaMnO_2 . *Phys. Rev. Lett.* **99**, 247211.
 12. Zorko, A., El Shawish, S., Arčon, D., Jagličić, Z., Lappas, A., Van Tol, H., and Brunel, L. C. (2008). Magnetic interactions in α - NaMnO_2 : Quantum spin-2 system on a spatially anisotropic two-dimensional triangular lattice. *Phys. Rev. B* **77**, 024412.
 13. Chen, X., Dong, J., and Li, X. (2020). A picture of pseudogap phase related to charge fluxes. *npj Comput. Mater.* **6**, 1–12.
 14. Bechtel, J. S., and Van Der Ven, A. (2018). Octahedral tilting instabilities in inorganic halide perovskites. *Phys. Rev. Mater.* **2**, 025401.
 15. Li, D., Lee, K., Wang, B. Y., Osada, M., Crossley, S., Lee, H. R., Cui, Y., Hikita, Y., and Hwang, H. Y. (2019). Superconductivity in an infinite-layer nickelate. *Nature* **572**, 624–

- 627.
16. Bussmann-Holder, A., Bishop, A. R., Migliori, A., and Fisk, Z. (1992). Role of structural instability in high-temperature superconductivity and its effect on isotope effect. *Ferroelectrics* **128**, 105–110.
 17. Bersuker, B. I. (2006). *The Jahn–Teller Effect*. (Cambridge Univ. Press).
 18. Goodenough, J. B. Jahn-Teller phenomena in solids. (1998). *Annu. Rev. Mater. Sci.* **28**, 1–27.
 19. Delmas, C., Braconnier, J.-J., Fouassier, C., and Hagemuller, P. (1981). Electrochemical intercalation of sodium in Na_xCoO_2 bronzes. *Solid State Ionics* **34**, 165–169.
 20. Chen, X. Wang, Y., Wiaderek, K., Sang, X., Borkiewicz, O., Chapman, K., LeBeau, J., Lynn, J., and Li, X. (2018). Super Charge Separation and High Voltage Phase in Na_xMnO_2 . *Adv. Funct. Mater.* **28**, 1805105.
 21. Kaufman, J. L., and Van Der Ven., A. (2019). Na_xCoO_2 phase stability and hierarchical orderings in the O3/P3 structure family. *Phys. Rev. Mater.* **3**, 015402.
 22. Toumar, A. J., Ong, S. P., Richards, W. D., Dacek, S., and Ceder, G. (2015). Vacancy ordering in O3-type layered metal oxide sodium-ion battery cathodes. *Phys. Rev. Appl.* **4**, 064002.
 23. de Boisse, B. M. (2014). Structural and electrochemical studies of $\text{Na}_x\text{Mn}_{1-y}\text{Fe}_y\text{O}_2$ and NaNiO_2 materials as positive electrode for Na-ion batteries. (Université de Bordeaux).
 24. Braconnier, J. J., Delmas, C., and Hagemuller, P. (1982). Etude par desintercalation electrochimique des systemes Na_xCrO_2 et Na_xNiO_2 . *Mater. Res. Bull.* **17**, 993–1000.
 25. Zhong, W., Vanderbilt, D., and Rabe, K. M. (1994). Phase transitions in BaTiO_3 from first principles. *Phys. Rev. Lett.* **73**, 1861–1864.

26. Cohen, R. E. (1992). Origin of ferroelectricity in perovskite oxides. *Nature* **358**, 136–138.
27. Ma, X., Chen, H., and Ceder, G. (2011). Electrochemical properties of monoclinic NaMnO₂. *J. Electrochem. Soc.* **158**, 1307–1312.
28. Vassilaras, P., Ma, X., Li, X., and Ceder, G. (2013). Electrochemical properties of monoclinic NaNiO₂. *J. Electrochem. Soc.* **160**, 207–211.
29. Lynn, J. W., Chen, Y., Chang, S., Zhao, Y., Chi, S., Ratcliff, W., Ueland, B. G., and Erwin, R. W. (2012). Double-focusing thermal triple-axis spectrometer at the NCNR. *J. Res. Natl. Inst. Stand. Technol.* **117**, 61–79.
30. Neufeind, J., Feygenson, M., Carruth, J., Hoffmann, R., and Chipley, K. K. (2012). The Nanoscale Ordered MAterials Diffractometer NOMAD at the Spallation Neutron Source SNS. *Nucl. Instruments Methods Phys. Res. Sect. B Beam Interact. with Mater. Atoms* **287**, 68–75.
31. Calder, S. *et al.* (2018). A suite-level review of the neutron powder diffraction instruments at Oak Ridge National Laboratory. *Rev. Sci. Instrum.* **89**, 092701.
32. Ikeda, S., and Carpenter, J. M. (1985). Wide-energy-range, high-resolution measurements of neutron pulse shapes of polyethylene moderators. *Nucl. Instruments Methods Phys. Res. Sect. A Accel. Spectrometers, Detect. Assoc. Equip.* **239**, 536–544.
33. Larson, A. C., and Von Dreele, R. B. (1994). Report LAUR, 86-748.
34. Young, R. A. (1993). *The Rietveld Method* (Oxford university press).
35. Wang, Y. *et al.* (2020). The range of non-Kitaev terms and fractional particles in α -RuCl₃. *npj Quantum Mater.* **5**, 1–8.
36. Kobayashi, W., Yanagita, A., Akaba, T., Shimono, T., Tanabe, D., and Moritomo, Y. (2018). Thermal expansion in layered Na_xMO₂. *Sci. Rep.* **8**, 3988.

37. Tian, Y. Jia, S., Cava, R. J., Zhong, R., Schneeloch, J., Gu, G., and Burch, K. S. (2017). Understanding the evolution of anomalous anharmonicity in $\text{Bi}_2\text{Te}_{3-x}\text{Se}_x$. *Phys. Rev. B* **95**, 094104.
38. Kim, S., Chen, X., Fitzhugh, W., and Li, X. (2018). Apical charge flux-modulated in-plane transport properties of cuprate superconductors. *Phys. Rev. Lett.* **121**, 157001.
39. Togo, A., and Tanaka, I. (2015). First principles phonon calculations in materials science. *Scr. Mater.* **108**, 1–5.

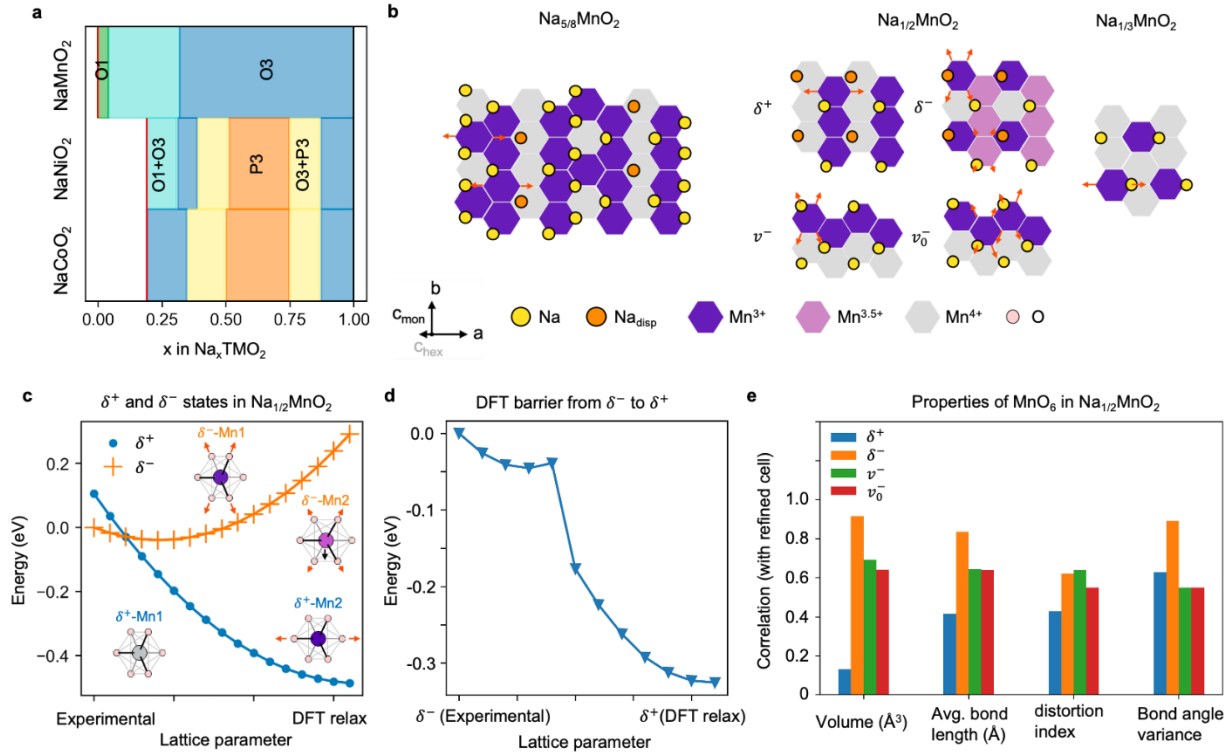
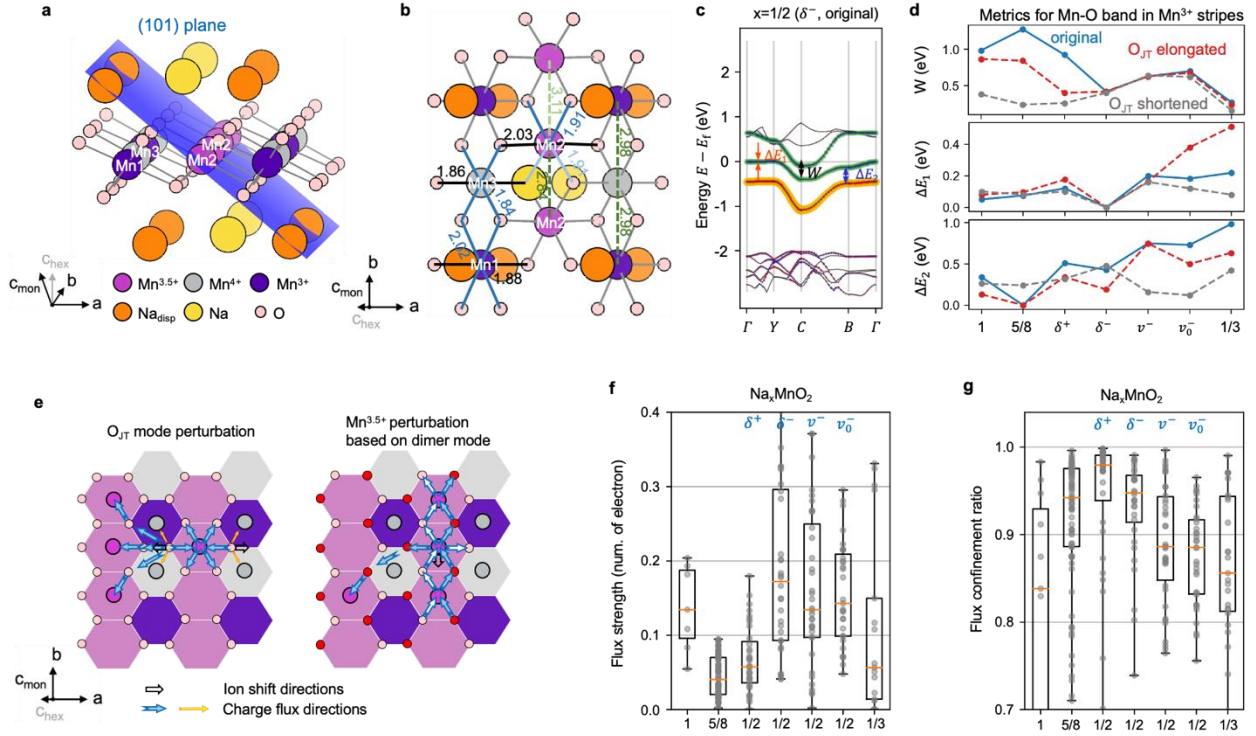


Figure 1. Phase evolution of Na_xTMO_2 (TM = Mn, Ni, Co) with Na composition (x) and abnormal JT distortions of O3- $\text{Na}_{1/2}\text{MnO}_2$. **a.** Phase diagrams of NaMnO_2 , NaNiO_2 and NaCoO_2 obtained from *in-situ* synchrotron XRD measurements (SI Fig S1 to S8). Black and red vertical lines on the boundaries mark the Na composition range in the *in-situ* measurements. **b.** Evolution of the Na and Mn charge orderings from $x = 5/8$ to $1/2$ and $1/3$ in Na_xMnO_2 . Four candidate structures δ^+ , δ^- , v^- , v_0^- are found in DFT simulations for $x = 1/2$. Jahn-Teller distortions are indicated by red arrows, with the distortion level illustrated using the arrow length. **c.** DFT energies of δ^+ and δ^- states in $\text{Na}_{1/2}\text{MnO}_2$. The lattice parameters are interpolated between experimental lattice parameters determined by *in-situ* SXR refinement and DFT fully relaxed lattice parameters of the δ^+ state. The main distortions of MnO_6 octahedra for the two states are illustrated by red arrows in insets. The black arrow indicates the $\text{Mn}^{3.5+}$ ion away from the perfect octahedron center to form the dimer in δ^- . **d.** DFT calculation of structures with gradually changing lattice parameters from the experimental value to the DFT fully relaxed value of δ^+ . Each image has fixed lattice parameters and the internal coordinates are relaxed. **e.** The correlation of the volumes, average bond lengths, distortion indices (measures the difference in Mn-O bond lengths) and bond angle variances of all the MnO_6 octahedra in $\text{Na}_{1/2}\text{MnO}_2$, between each of the four DFT candidate states and the state from *in-situ* SXR refinement of both internal coordinates and lattice parameters, all at experimental lattice parameters.



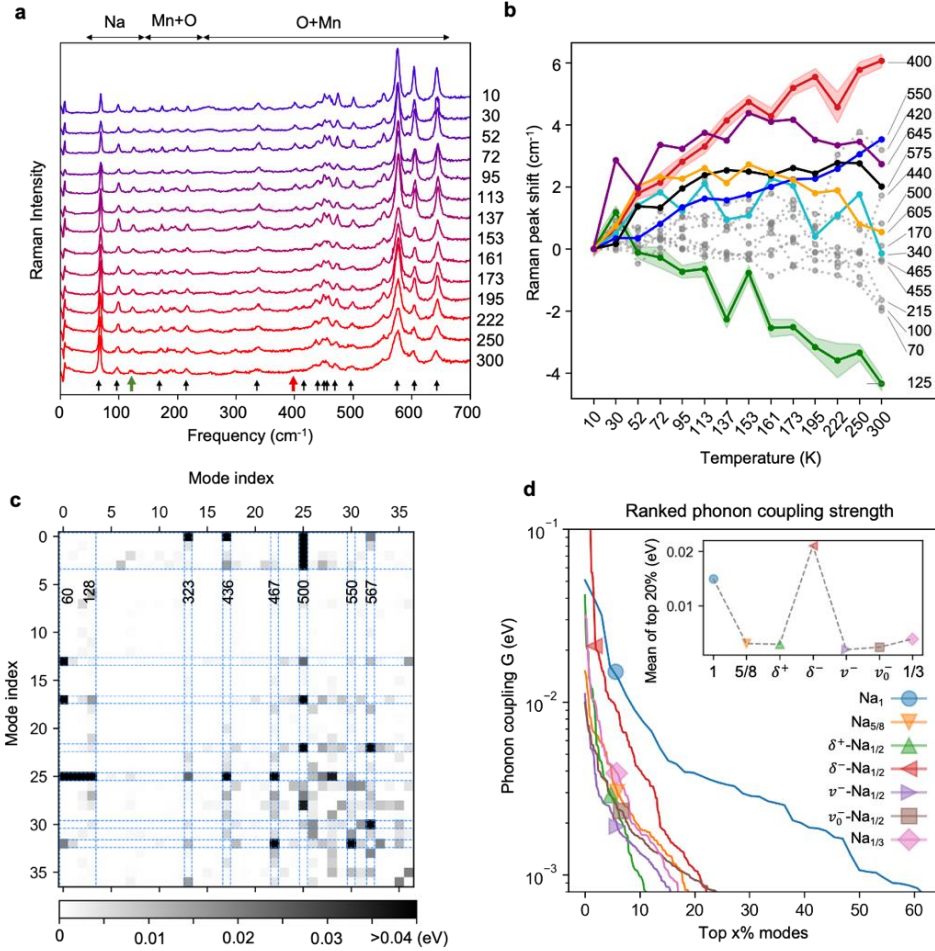


Figure 3. Strong anharmonic phonon coupling in $\text{Na}_{1/2}\text{MnO}_2$. **a.** Raman measurements for $\text{Na}_{1/2}\text{MnO}_2$ cooling from 300K to 10K. The 16 Raman peaks marked by black, green and red arrows are selected for further analysis. Green and red arrows indicate two Raman peaks with significant shifts in frequency with decreasing temperature (SI Fig. S17). Three typical frequency ranges dominated by different phonon modes are determined by comparing with DFT simulations and labelled at the top, with Na modes at low frequencies, Mn dominant modes mixed with minor oxygen modes at intermediate frequencies (Mn+O), and O dominant modes mixed with minor Mn modes (O+Mn) at high frequencies. **b.** Raman peak frequency shift with temperature, relative to the value at 10K, for peaks marked in (a). The volume expansion effect has been subtracted. The shaded regions represent the standard deviation from measurements and peak position calculations. The modes with frequencies $> 300 \text{ cm}^{-1}$ involve a positive peak shift in certain temperature ranges. **c.** Nonlinear phonon coupling between 37 modes of the δ^- state. Darker grey scale indicates stronger phonon coupling. The blue dashed stripes mark the modes with strongest anharmonic phonon couplings to other modes, with their frequencies (in cm^{-1}) labeled. The phonon coupling maps for all seven Na_xMnO_2 states are shown in SI Fig. S20. **d.** Comparison of the phonon coupling spectra of all seven Na_xMnO_2 . The mode pairs are ranked from highest to lowest phonon coupling strength G for each state. The markers indicate the average phonon coupling strength of the top 20% mode pairs for each state, which are summarized in the inset.

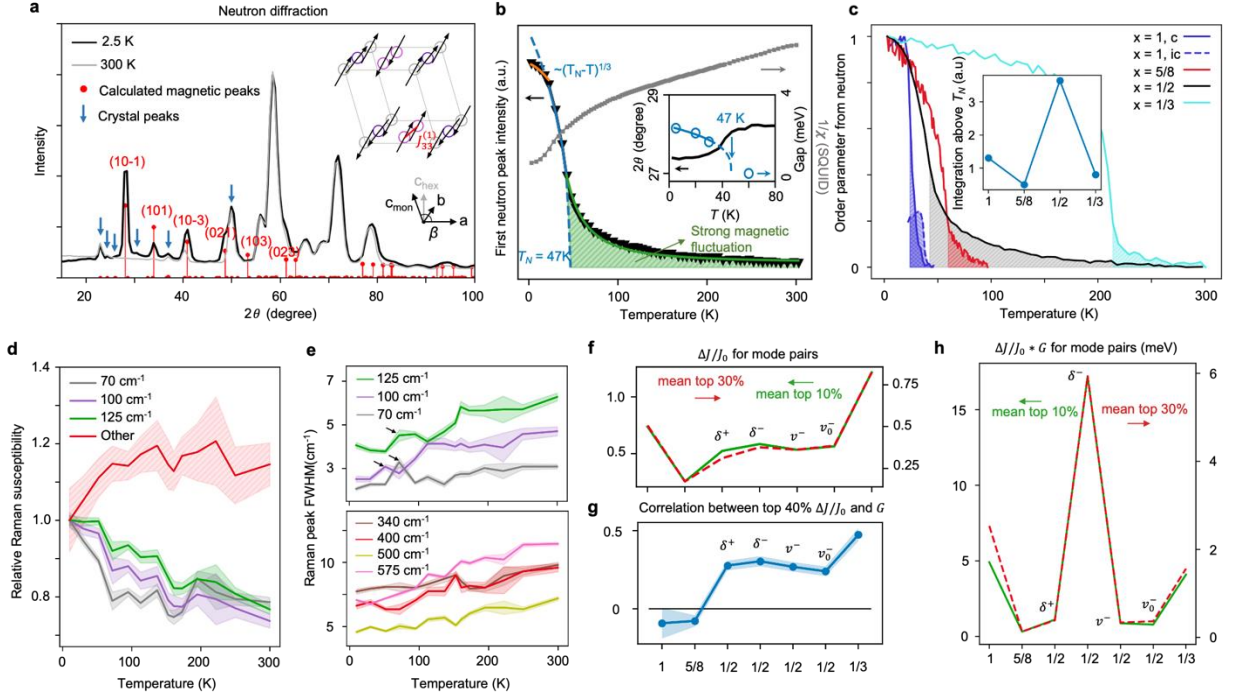


Figure 4. Strong magnetic fluctuations synchronized with anharmonic phonon couplings in $\text{Na}_{1/2}\text{MnO}_2$. **a.** Neutron diffraction patterns at 2.5 K (black) and 300 K (grey). Calculated magnetic peaks are labelled by red lines. Inset illustrates the magnetic moments obtained from neutron diffraction refinement. Major crystal peaks are labelled by blue arrows. The magnetic unit cell consists of two layers of Mn spins, with AFM interlayer stacking. **b.** Energy integrated intensity (black triangle), including magnetic fluctuations (green area), of the (10-1) strongest magnetic peak (left scale) and the inverse magnetic susceptibility (grey line, right scale) versus temperature. The order parameter of the region right below T_N is fitted with the $(T_N - T)^{1/3}$ power law (blue dashed line). Also see SI Fig. S22 for the order parameter fit. Inset shows the weighted average (10-1) peak position (black line), and the magnon gap (blue circle) measured by inelastic neutron scattering (also see SI Fig. S25), both versus temperature. **c.** Order parameters from neutron diffraction vs. temperature compared with Na_xMnO_2 for $x = 1, 5/8$, and $1/3$. Inset shows the comparison of integrated shade area above T_N . The $x = 1, 5/8$ and $1/3$ data are reproduced from Refs. 10, 7, 20, respectively. Both commensurate (c) and incommensurate (ic) residue intensities are integrated for the inset point at $x = 1$. **d.** Raman susceptibility versus temperature. The shaded regions for the bottom three modes represent the error bar. The shaded region with red lines marks the range of all other high frequency modes. **e.** Full-width-half-maximum (FWHM) of two groups of Raman peaks around low (top) and high (bottom) frequencies, respectively, versus temperature. Shaded region corresponds to the error. **f.** The strongest relative J change, $\Delta J/J_0$, induced by any pairs of phonon modes at zero point amplitude. **g.** Correlation between mode pairs with both the top 40% $\Delta J/J_0$ and G for each structure. Shaded area shows the error bar of the correlation. **h.** The product of $\Delta J/J_0$ and corresponding phonon coupling strength G . (f) and (h) compare the δ^- state with all other Na_xMnO_2 for the mean top 10% (green) and 30% (red) mode pairs.